Simulations of Blood Flow on the Cell Scale

Dmitry A. Fedosov

Theoretical and Soft Matter Biophysics, Institute of Complex Systems and Institute for Advanced Simulation,
Research Centre Jülich, 52425 Jülich, Germany
E-mail: d.fedosov@fz-juelich.de

Red blood cells (RBCs) in various flows exhibit a rich dynamics due their deformability and govern rheological properties and flow characteristics of human blood. Using a mesoscopic RBC model which incorporates membrane shear elasticity, bending rigidity, and viscosity, we quantitatively predict the behavior of a single RBC in shear flow and the dependence of blood viscosity on shear rate and hematocrit. In shear flow, single RBCs respond by tumbling at low shear rates and tank-treading at high shear rates. In transitioning between these regimes, the membrane exhibits substantial deformation controlled largely by flexural stiffness. In RBC suspension (blood) under shear, not only the tumbling/tank-treading cell dynamics affects blood flow characteristics, but also RBC collective behavior and cell-cell aggregation interactions. RBC aggregation leads to reversible rouleaux structures and a tremendous increase of blood viscosity at low shear rates, and results in the presence of a yield stress. The non-Newtonian behavior of blood is analyzed and related to the suspension's microstructure, deformation and dynamics of single RBCs. The generality of these cell models suggests that they can easily be adapted to tune the properties of a much wider class of complex fluids including capsule and vesicle suspensions.

1 Introduction

Blood is circulated around the entire body performing a number of physiological functions. Its main functions are the transport of oxygen and nutrients to cells of the body, removal of waste products such as carbon dioxide and urea, and circulation of molecules and cells which mediate the organism's defense and immune response and play a fundamental role in the tissue repair process. Abnormal blood flow is often correlated with a broad range of disorders and diseases which include hypertension, anemia, atherosclerosis, malaria, and thrombosis. Understanding the rheological properties and dynamics of blood cells and blood flow is crucial for many biomedical and bioengineering applications. Examples include the development of blood substitutes, the design of blood flow assisting devices, and drug delivery. In addition, understanding of vital blood related processes in health and disease may aid in the development of new effective treatments.

Blood is a physiological fluid that consists of erythrocytes or red blood cells (RBCs), leukocytes or white blood cells (WBCs), thrombocytes or platelets, and plasma containing various molecules and ions. RBCs constitute approximately 45% of the total blood volume, WBCs around 0.7%, and the rest is taken up by blood plasma and its substances. One microliter of blood contains about 5 million RBCs, roughly 5 thousand WBCs, and approximately a quarter million platelets. Due to a high volume fraction of RBCs, the rheological properties of blood are mainly determined by their properties and interactions.

Modern rheometry techniques are able to reliably measure macroscopic properties of cell suspensions, for instance the bulk viscosity of blood[1–3]. At low shear rates the RBCs in whole blood have been observed to aggregate into structures called "rouleaux", which

resemble stacks of coins[1,4,5]. The aggregation process appears to be strongly correlated to the presence of the plasma proteins[4,5]. Experiments with washed RBCs re-suspended in pure saline to which fibrinogen was added progressively[4] showed a tremendous viscosity increase at low deformation rates with respect to fibrinogen concentration. In addition, such suspensions exhibit a yield stress[1,6,7], i.e., a threshold stress for flow to begin.

These experimental advances have not been accompanied by theoretical developments which can yield quantitative predictions of rheological and flow properties of blood. A number of theoretical and numerical analyses have sought to describe cell behavior and deformation in a variety of flows. Examples include models of ellipsoidal cells enclosed by viscoelastic membranes[8,9], numerical models based on shell theory[10–12], and discrete descriptions at a mesoscopic level[13–16]. Mesoscopic modeling of viscoelastic membranes is developing rapidly with a RBC membrane modeled as a network of viscoelastic springs in combination with a membrane flexural stiffness, and constraints on the surface area and volume[13–16]. However, recent theoretical and numerical studies focused mostly on the behavior of a single RBC in various flows[13,8,16]. Several studies have also been performed to simulate a suspension of multiple cells[17–19] in tube flow.

In this chapter, a theoretical analysis will be presented for a membrane network model exhibiting specified macroscopic membrane properties without parameter adjustment. RBC dynamics in shear flow showing tumbling and tank-treading will be studied in detail with a view to delineating the effect of the membrane shear moduli, bending rigidity, external, internal, and membrane viscosities. Comparison with available experiments will demonstrate that the computational model is able to accurately describe realistic RBC dynamics in shear flow. Comparison of the numerical simulations with theoretical predictions[8,9] will reveal discrepancies suggesting that the current theoretical models are only qualitatively accurate due to strong simplifications.

Moreover, we will examine blood rheological properties of modeled RBC suspension. In particular, we will investigate the effect of RBC aggregation on blood viscosity, reversible rouleaux formation, and yield stress in a RBC suspension[20]. In addition, we will establish the connection between the rheology of a cell suspension and its microscopic properties on a single-cell level, such as structure or arrangement, cell viscoelastic properties, and local dynamics. In conclusion, we will focus on the *quantitative* prediction of rheological properties and dynamics of single RBCs and blood flow.

2 Red blood cells

A healthy human RBC has a biconcave shape with an average diameter of approximately $7.82\ \mu m$. Figure 1 shows a schematic of a RBC membrane which consists of a lipid bilayer with an attached cytoskeleton formed by a network of the spectrin proteins linked by short filaments of actin. The lipid bilayer is considered to be a nearly viscous and area preserving membrane[10], while RBC elasticity is attributed to the attached spectrin network, as is the integrity of the entire RBC when subjected to severe deformations in the capillaries as small as $3\ \mu m$. The RBC membrane encloses a viscous cytosol whose viscosity is several times larger than that of blood plasma under physiological conditions. Mechanical and rheological characteristics of RBCs and their dynamics are governed by: membrane elastic and viscous properties, bending resistance, and the viscosities of the external/internal fluids.

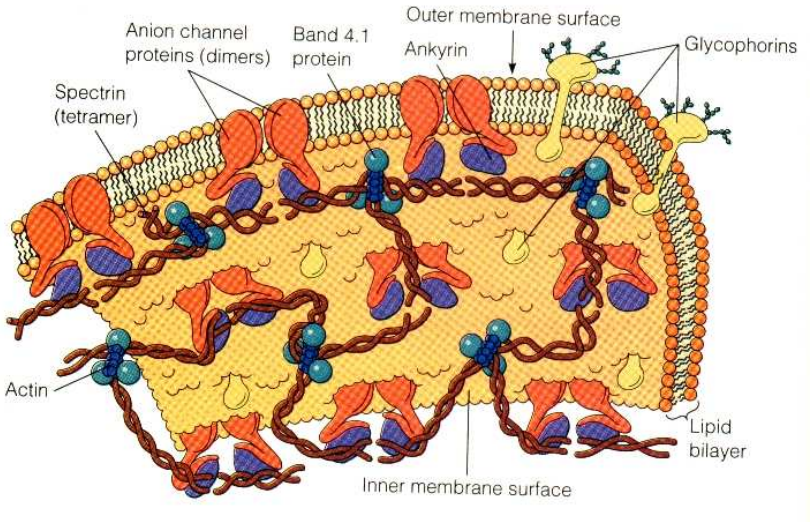

Figure 1. A schematic of the RBC membrane structure.

3 Methods and models

In the model, the RBC membrane is represented by a viscoelastic network. The motion of the membrane and of the internal and external fluids is described by the method of dissipative particle dynamics (DPD)[21], a mesoscopic particle-based simulation technique, see appendix A for details.

3.1 Red blood cell membrane

The RBC membrane is represented by N_v DPD particles with coordinates $\{\mathbf{x}_{i=1\ldots N_v}\}$ which are vertices of a two-dimensional triangulated network on the RBC surface[22, 16, 23], as shown in figure 2. The network has a fixed connectivity with the energy as follows

$$U(\{\mathbf{x}_i\}) = U_s + U_b + U_{a+v}, \tag{1}$$

where U_s is the spring's potential energy, U_b is the bending energy, and U_{a+v} corresponds to the area and volume conservation constraints. The U_s contribution provides membrane elasticity similar to that of a spectrin network of RBC membrane. A "dashpot" is attached to each spring, and therefore, the spring forces are a combination of conservative elastic forces and dissipative forces, which provide network viscous response similar to RBC membrane viscosity. The bending energy mimics bending resistance of the RBC membrane, while the area and volume conservation constraints mimic area-incompressibility of the lipid bilayer and incompressibility of a cytosol, respectively. Below, these energies are described in detail.

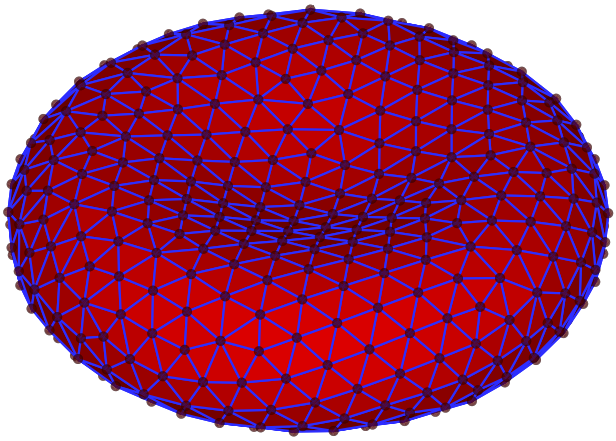

Figure 2. A sketch of a RBC membrane network.

The network nodes are connected by N_s springs with the potential energy as follows

$$U_s = \sum_{j \in 1...N_s} \left[\frac{k_B T l_m (3x_j^2 - 2x_j^3)}{4p(1-x_j)} + \frac{k_p}{(n-1) l_j^{n-1}} \right], \tag{2}$$

where l_j is the length of the spring j, l_m is the maximum spring extension, $x_j = l_j / l_m$, p is the persistence length, $k_B T$ is the energy unit, k_p is the spring constant, and n is a power. The above equation includes the attractive wormlike chain potential and a repulsive potential for $n > 0$ such that a non-zero equilibrium spring length can be imposed. The performance of different spring models for the RBC membrane was studied in Ref.[23] in detail.

To incorporate the membrane viscosity into the RBC model a dissipative force is introduced for each spring. Following the general framework of the fluid particle model[24] we can define dissipative $\mathbf{F}_{ij}^D$ and random $\mathbf{F}_{ij}^R$ forces for each spring, where $i, j \in 1...N_v$ are a pair of two network vertices connected by a spring. Such forces satisfy the fluctuation-dissipation balance providing consistent temperature of the RBC membrane in equilibrium and are given by

$$\mathbf{F}_{ij}^D = -\gamma^T \mathbf{v}_{ij} - \gamma^C (\mathbf{v}_{ij} \cdot \mathbf{e}_{ij}) \mathbf{e}_{ij}, \tag{3}$$

$$\mathbf{F}_{ij}^R dt = \sqrt{2k_B T} \left(\sqrt{2\gamma^T} d\overline{\mathbf{W}_{ij}^S} + \sqrt{3\gamma^C - \gamma^T} \frac{tr[d\mathbf{W}_{ij}]}{3} \mathbf{1} \right) \cdot \mathbf{e}_{ij}, \tag{4}$$

where γ^T and γ^C are dissipative parameters and the superscripts T and C denote the "translational" and "central" components, $\mathbf{v}_{ij}$ is the relative velocity of spring ends, $tr[d\mathbf{W}_{ij}]$ is the trace of a random matrix of independent Wiener increments $d\mathbf{W}_{ij}$, and

$d\overline{\mathbf{W}_{ij}^S} = d\mathbf{W}_{ij}^S - tr[d\mathbf{W}_{ij}^S]\mathbf{1}/3$ is the traceless symmetric part. Note that the condition $3\gamma^C - \gamma^T \geq 0$ has to be satisfied.

The bending energy of the RBC membrane is given as follows

$$U_b = \sum_{j \in 1 \ldots N_s} k_b \left[1 - cos(\theta_j - \theta_0)\right], \tag{5}$$

where k_b is the bending constant, θ_j is the instantaneous angle between two adjacent triangles having the common edge j, and θ_0 is the spontaneous angle.

In addition, the RBC model includes the area and volume conservation constraints with the corresponding energy given by

$$U_{a+v} = \sum_{j \in 1 \ldots N_t} \frac{k_d (A_j - A_0)^2}{2A_0} + \frac{k_a (A - A_0^{tot})^2}{2A_0^{tot}} + \frac{k_v (V - V_0^{tot})^2}{2V_0^{tot}}, \tag{6}$$

where N_t is the number of triangles in the membrane network, A_0 is the triangle area, and k_d, k_a and k_v are the local area, global area and volume constraint coefficients, respectively. The terms A and V are the total RBC area and volume, while A_0^{tot} and V_0^{tot} are the specified total area and volume, respectively. More details on the RBC model can be found in Refs.[16,23].

3.2 Membrane macroscopic properties

Several parameters must be chosen in the membrane network model to ensure a desired mechanical response. Figure 3 depicts a network model and its continuum counterpart. To

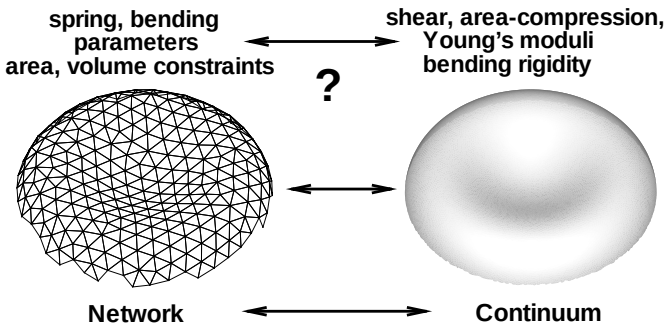

Figure 3. Illustration of a membrane network and corresponding continuum model.

circumvent ad-hoc parameter adjustment, we derive relationships between local model parameters and network macroscopic properties for an elastic hexagonal network. A similar analysis for a two-dimensional particulate sheet of equilateral triangles was presented in Refs.[25,23].

Figure 4 illustrates an element in a hexagonal network with vertex **v** placed at the origin of a local Cartesian system. Using the virial theorem[26], we find that the Cauchy

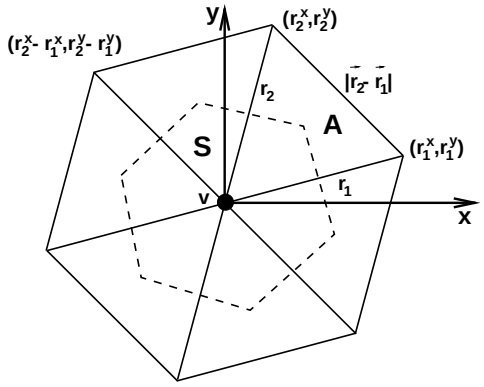

Figure 4. Illustration of an element in a hexagonal triangulation.

stress tensor at **v** is

$$\tau_{\alpha\beta} = -\frac{1}{S}\left[\frac{f(r_1)}{r_1}r_1^\alpha r_1^\beta + \frac{f(r_2)}{r_2}r_2^\alpha r_2^\beta + \frac{f(|\boldsymbol{r}_2-\boldsymbol{r}_1|)}{|\boldsymbol{r}_2-\boldsymbol{r}_1|}(r_2^\alpha - r_1^\alpha)(r_2^\beta - r_1^\beta)\right] - \left(\frac{k_a(A_0^{tot}-N_tA)}{A_0^{tot}} + \frac{k_d(A_0-A)}{A_0}\right)\delta_{\alpha\beta}, \quad (7)$$

where α and β stand for x or y, $f(r)$ is the spring force, $A_0^{tot} = N_t A_0$, $S = 2A_0$, $\delta_{\alpha\beta}$ is the Kronecker delta, and S is the area of the hexagonal element centered at **v**.

3.2.1 Shear modulus

The shear modulus is derived from the network deformation by applying a small engineering shear strain γ to the network element shown in figure 4. For instance, the deformation of a material vector $\boldsymbol{r}_1$ is then described as

$$\boldsymbol{r}_1' = \boldsymbol{r}_1 \cdot \boldsymbol{J} = \begin{bmatrix} r_1^x + \frac{1}{2}r_1^y \\ \frac{1}{2}r_1^x\gamma + r_1^y \end{bmatrix}, \quad (8)$$

where

$$\boldsymbol{J} = \begin{bmatrix} 1 & \gamma/2 \\ \gamma/2 & 1 \end{bmatrix} + O(\gamma^2) \quad (9)$$

is the linear strain tensor and $\boldsymbol{r}_1 = (r_1^x; r_1^y)$, as shown in figure 4. Because the shear deformation is area preserving, only spring forces in equation (7) contribute to the membrane shear modulus.

Expanding τ_{xy} in a Taylor series, we find that

$$\tau_{xy}' = \tau_{xy} + \left.\frac{\partial \tau_{xy}'}{\partial \gamma}\right|_{\gamma=0}\gamma + O(\gamma^2). \quad (10)$$

The linear shear modulus of the network is

$$\mu_0 = \left. \frac{\partial \tau'_{xy}}{\partial \gamma} \right|_{\gamma=0}. \tag{11}$$

For example, differentiating the first term of τ_{xy} in equation (7) yields

$$\frac{\partial}{\partial \gamma} \left(\frac{f(r'_1)}{r'_1} r_1^{x'} r_1^{y'} \right)_{\gamma=0} = \left(\frac{\partial \frac{f(r_1)}{r_1}}{\partial r_1} \frac{(r_1^x r_1^y)^2}{r_1} + \frac{f(r_1) r_1}{2} \right)_{r_1=l_0}, \tag{12}$$

where l_0 is the equilibrium spring length. Using the vector-product definition of the area of a triangle, we obtain

$$(r_1^x r_1^y)^2 + (r_2^x r_2^y)^2 + (r_2^x - r_1^x)^2 (r_2^y - r_1^y)^2 = 2A_0^2. \tag{13}$$

The linear shear modulus of the network model is

$$\mu_0 = \frac{\sqrt{3} k_B T}{4 p l_m x_0} \left(\frac{x_0}{2(1-x_0)^3} - \frac{1}{4(1-x_0)^2} + \frac{1}{4} \right) + \frac{\sqrt{3} k_p (n+1)}{4 l_0^{n+1}}, \tag{14}$$

where $x_0 = l_0 / l_m$.

3.2.2 Area compression and Young's moduli

The linear elastic area compression modulus K is found from the in-plane pressure following a small area expansion as

$$p = -\frac{1}{2}(\tau_{xx} + \tau_{yy}) = \frac{3\,l}{4A} f(l) + \frac{(k_a + k_d)(A_0 - A)}{A_0}. \tag{15}$$

Defining the compression modulus as

$$K = -\frac{\partial p}{\partial \log A}\Big|_{A=A_0} = -\frac{1}{2} \frac{\partial p}{\partial \log l}\Big|_{l=l_0} = -\frac{1}{2} \frac{\partial p}{\partial \log x}\Big|_{x=x_0}, \tag{16}$$

and using equations (15) and (16), we obtain

$$K = 2\mu_0 + k_a + k_d. \tag{17}$$

For the nearly constant-area membrane enclosing a red blood cell, the compression modulus is much larger than the shear elastic modulus μ_0.

The Young's modulus of the two-dimensional sheet is given by

$$Y = \frac{4K\mu_0}{K + \mu_0}. \tag{18}$$

As $K \to \infty$, we obtain $Y \to 4\mu_0$. To ensure a nearly constant area, we set $k_a + k_d \gg \mu_0$.

3.2.3 Bending rigidity

Helfrich[27] proposed an expression for the bending energy of a lipid membrane,

$$E_c = \frac{k_c}{2} \iint (C_1 + C_2 - 2C_0)^2 \, dA + k_g \iint C_1 C_2 \, dA, \tag{19}$$

where C_1 and C_2 are the principal curvatures, C_0 is the spontaneous curvature, and k_c, k_g are bending rigidities. The second term on the right-hand side of equation (19) is constant for any closed surface.

A relationship between the bending constant, k_b, and the macroscopic membrane bending rigidity, k_c, can be derived for a spherical shell. Figure 5 shows two equilateral triangles with edge length l_0 whose vertices lie on a sphere of radius R. The angle between the tri-

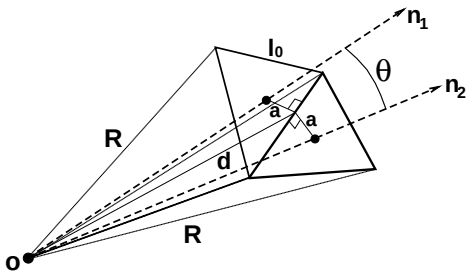

Figure 5. Illustration of two equilateral triangles on the surface of a sphere of radius R.

angle normals $\mathbf{n}_1$ and $\mathbf{n}_2$ is denoted by θ. In the case of a spherical shell, the total energy in equation (19) is found to be

$$E_c = 8\pi k_c \left(1 - \frac{C_0}{C_1}\right)^2 + 4\pi k_g = 8\pi k_c \left(1 - \frac{R}{R_0}\right)^2 + 4\pi k_g, \tag{20}$$

where $C_1 = C_2 = 1/R$ and $C_0 = 1/R_0$. In the network model, the bending energy of the triangulated sphere is

$$U_b = N_s \, k_b \, [1 - \cos(\theta - \theta_0)]. \tag{21}$$

Expanding $\cos(\theta - \theta_0)$ in a Taylor series around $\theta - \theta_0$ provides us with the leading term

$$U_b = \frac{1}{2} N_s k_b (\theta - \theta_0)^2 + O\left((\theta - \theta_0)^4\right). \tag{22}$$

With reference to figure 5, we find that $2a \approx \theta R$ or $\theta = l_0/(\sqrt{3}R)$, and $\theta_0 = l_0/(\sqrt{3}R_0)$.

For a sphere, $A = 4\pi R^2 \approx N_t A_0 = \sqrt{3} N_t l_0^2/4 = \sqrt{3} N_s l_0^2/6$, and $l_0^2/R^2 = 8\pi\sqrt{3}/N_s$. Finally, we obtain

$$U_b = \frac{1}{2} N_s k_b \left(\frac{l_0}{\sqrt{3}R} - \frac{l_0}{\sqrt{3}R_0}\right)^2 = \frac{N_s k_b l_0^2}{6R^2} \left(1 - \frac{R}{R_0}\right)^2 = \frac{4\pi k_b}{\sqrt{3}} \left(1 - \frac{R}{R_0}\right)^2. \tag{23}$$

Equating the macroscopic bending energy E_c to U_b for $k_g = -4k_c/3$ and $C_0 = 0$, we obtain $k_b = 2k_c/\sqrt{3}$ in agreement with the limit of a continuum approximation[28].

The spontaneous angle θ_0 is set according to the total number of vertices on the sphere, N_v. It can be shown that $\cos\theta = 1 - 1/[6(R^2/l_0^2 - 1/4)]$ and the number of sides is $N_s = 2N_v - 4$. The bending coefficient, k_b, and spontaneous angle, θ_0, are given by

$$k_b = \frac{2}{\sqrt{3}}\, k_c, \qquad \theta_0 = \arccos\left(\frac{\sqrt{3}(N_v - 2) - 5\pi}{\sqrt{3}(N_v - 2) - 3\pi}\right). \tag{24}$$

3.2.4 Membrane viscosity

Since interparticle dissipative interaction is an intrinsic part of the DPD formulation, incorporating dissipative and random forces into springs fits naturally into the DPD scheme. The general framework of the fluid-particle model[24] provides us with equations (3) and (4). These dissipative and random forces in combination with an elastic spring constitute a mesoscopic viscoelastic spring. To relate the membrane shear viscosity, η_m, to the model dissipative parameters γ^T and γ^C, an element of the hexagonal network shown in figure 4 is subjected to a constant shear rate, $\dot{\gamma}$. The shear stress τ_{xy} at short times can be approximated from the contribution of the dissipative force in equation (3),

$$\tau_{xy} = -\frac{1}{2A_0}\Big[\gamma^T\dot{\gamma}\left((r_y^1)^2 + (r_y^2)^2 + (r_y^2 - r_y^1)^2\right) + \frac{\gamma^C\dot{\gamma}}{l_0^2}\Big(\,(r_x^1 r_y^1)^2 + (r_x^2 r_y^2)^2 + (r_x^2 - r_x^1)^2(r_y^2 - r_y^1)^2\,\Big)\Big] = \dot{\gamma}\,\sqrt{3}\,(\gamma^T + \frac{1}{4}\,\gamma^C\,). \tag{25}$$

The membrane viscosity is given by

$$\eta_m = \frac{\tau_{xy}}{\dot{\gamma}} = \sqrt{3}\,\left(\gamma^T + \frac{1}{4}\,\gamma^C\right). \tag{26}$$

This equation indicates that γ^T accounts for the largest portion of the membrane dissipation. Therefore, γ^C is set to its minimum value, $\frac{1}{3}\,\gamma^T$, in the simulations.

3.3 Membrane-solvent interfacial conditions

The cell membrane encloses a viscous fluid and is surrounded by a liquid solvent. Figure 6 shows a snapshot of a simulation in equilibrium, where red particles are membrane vertices, blue particles represent the external fluid, and green particles represent the internal fluid. To prevent mixing of the internal and external fluids, we require impenetrability. We also enforce no-slip boundary conditions at the membrane implemented by pairwise interactions between fluid particles and membrane nodes. Bounce-back reflection of fluid particles at the triangular plaquettes satisfies membrane impenetrability and better enforces no-slip compared to specular reflection. However, bounce-back reflection alone does not guarantee no-slip. In practice, it is necessary to properly set the DPD dissipative interactions between fluid particles and membrane vertices.

The continuum linear shear flow over a flat plate is used to determine the dissipative force coefficient γ for the fluid-membrane coupling. For the continuum, the total shear force on area A of the plate is $A\eta_0\dot{\gamma}$, where η_0 is the fluid viscosity and $\dot{\gamma}$ is the local

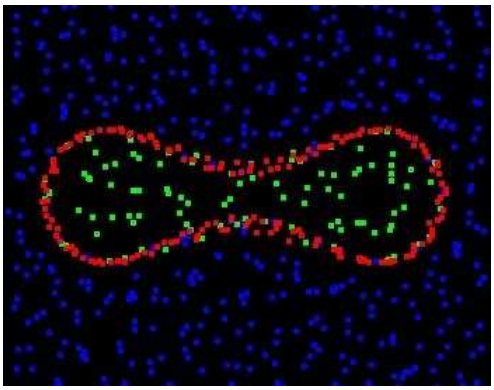

Figure 6. A slice through a sample equilibrium simulation. Red particles are membrane vertices, blue particles represent the external fluid, and green particles represent the internal fluid.

shear-rate. To mimic the membrane surface, wall particles are distributed over the plate to match the configuration of the cell network model. The force on a single wall particle in this system exerted by the surrounding fluid under shear can be expressed as

$$F_v = \iiint_{V_h} n\, g(r)\, F^D\, dV, \tag{27}$$

where F^D is the DPD dissipative force between fluid and wall particles, n is the fluid number density, $g(r)$ is the radial distribution function of fluid particles relative to the wall particles, and V_h is the half-sphere volume of fluid above the plate. Thus, the total shear force on the area A is equal to $N_A F_v$, where N_A is the number of plate particles residing in the area A. When conservative interactions between fluid particles and the membrane vertices are neglected, the radial distribution function simplifies to $g(r) = 1$. Setting $N_A F_v = A\eta_0\dot{\gamma}$ yields an expression for the dissipative force coefficient γ in terms of the fluid density and viscosity and the wall density, N_A/A. Near a wall where the half-sphere lies within the range of the linear wall shear flow, the shear rate cancels out. This formulation has been verified to enforce satisfactory no-slip boundary conditions for shear flow over a flat plate, and is an excellent approximation for no-slip at the membrane surface.

3.4 RBC aggregation interactions

For blood, the attractive cell-cell interactions are crucial for simulation of RBC aggregation into rouleaux. These forces are approximated phenomenologically with a Morse potential,

$$U_M(r) = D_e \left[e^{2\beta(r_0 - r)} - 2e^{\beta(r_0 - r)} \right], \tag{28}$$

where r is the separation distance, r_0 is the zero force distance, D_e is the well depth of the potential, and β characterizes the interaction range. The Morse potential interactions are implemented between every two vertices of separate RBCs if they are within a defined potential cutoff radius r_d. Eventhough the Morse potential in equation (28) contains a

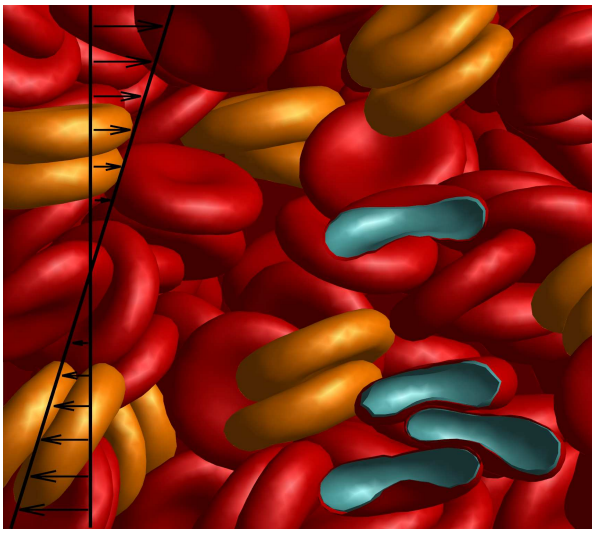

Figure 7. Simulation of whole blood under shear flow. RBCs are shown in red and in orange, where orange color depicts the rouleaux structures formed due to aggregation interactions between RBCs. The image also displays several cut RBCs with the inside drawn in cyan to illustrate RBC shape and deformability.

short-range repulsive force when $r < r_0$, such repulsive interactions cannot prevent two RBCs from an overlap. To guarantee no overlap among RBCs we employ a short range Lennard-Jones potential and specular reflections of RBC vertices on membranes of other RBCs. The specular reflections of RBC vertices on surfaces of other RBCs are necessary due to coarseness of the triangular network which represents the RBC membrane.

4 Simulation results and discussion

We present simulation results for the behavior of a single RBC in shear flow and discuss the effect of various membrane properties on RBC dynamics. We also study dense RBC suspension (blood) under shear and examine the blood viscosity with and without RBC aggregation, rouleaux formation, and yield stress. Finally, we establish a link between bulk blood properties, microstructure, and the flow behavior of single RBCs.

4.1 Simulation setup and parameters

A single RBC or the RBC suspension were subjected to linear shear flow with periodic Lees-Edwards boundary conditions[29] as shown in figure 7. The computational domain had the size of $5.6D_0 \times 4.0D_0 \times 3.4D_0$, where D_0 is the RBC diameter which is equal to about $7.82\ \mu m$ for a healthy RBC. In case of the RBC suspension, 168 RBCs and 117599 solvent particles were placed in the computational domain. The RBC membrane Young's modulus was set to $Y_0 = 269924\, k_BT/D_0^2$, which corresponds to $Y_0 = 18.9\, \mu N/m$ at physiological temperature of $T = 37^o\, C$. The RBC bending rigidity was assumed to be $k_c = 3{\times}10^{-19} J$, which is equal to approximately $70 k_BT$ at $T = 37^o\ C$. The corresponding Föppl-von

Kármán number $0.25 Y_0 D_0^2/k_c$ is therefore equal to approximately 963. The membrane viscosity was set to be $12\eta_0$, where η_0 is the suspending fluid viscosity. The coefficients for the area and volume constraints were set large enough in order to closely approximate membrane and cytosol incompressibility. Coupling between the solvent and RBCs was performed through a dissipative force between fluid particles and membrane vertices.

Interactions between different RBCs included the short range repulsive Lennard-Jones potential with parameters $\epsilon = 10.0\ k_B T$ and $\sigma_{LJ} = 0.037\ D_0$. These repulsive interactions result in a thin layer next to a RBC membrane which cannot be accessed by other cells. This layer can be interpreted as a slight increase of the RBC volume. Therefore, the RBC volume was assumed to be about 10% larger than that of the triangulated network. The concentration of RBCs is called hematocrit and denoted as H_t. RBC aggregation interactions were mediated by the Morse potential with parameters $D_e = 3.0\ k_B T$, $r_0 = \sigma_{LJ}$, $\beta = 0.45\ \sigma_{LJ}^{-1}$, and $r_d = 3.7\ \sigma_{LJ}$. For more details see Ref.[20].

4.2 Single RBC in shear flow

Experimental observations have shown that RBCs tumble at low shear rates and exhibit a tank-treading motion at high shear rates[30–32,8]. Fischer[31] attributed this behavior to a minimum elastic energy state of the cell membrane. Cells can be made to tank-tread in the laboratory for several hours. When the flow is stopped, the cells relax to the original biconcave shape where attached microbeads recover their original relative position. It appears that tank-treading is possible only when a certain elastic energy barrier has been surpassed. Theoretical analyses have considered ellipsoidal cell models tank-treading along a fixed ellipsoidal path[8,9]. Our simulations show that the dynamics depends on the membrane shear modulus, shear rate, and viscosity ratio $\lambda = (\eta_i + \eta_m)/\eta_o$, where η_i, η_m, and η_o are the interior, membrane, and outer fluid viscosities.

For viscosity ratio $\lambda < 3$, the theory predicts tumbling at low shear rates and tank-treading motion at high shear rates[9]. The cells exhibit an unstable behavior in a narrow intermittent region around the tumbling-to-tank-treading transition where tumbling can be followed by tank-treading and *vice versa*. For $\lambda > 3$, stable tank-treading does not necessarily arise. RBCs with viscosity ratio $\lambda > 3$ have been observed to tank-tread while exhibiting a swinging motion with a certain frequency and amplitude about an average tank-treading axis. The reliability of the theoretical predictions will be judged by comparison with the results of our simulations.

A RBC is suspended in a linear shear flow. The viscosities of the external solvent and internal cytosol fluid are set to $\eta_o = \eta_i = 0.005\ Pa \cdot s$, while the membrane viscosity is set to $\eta_m = 0.022\ Pa \cdot s$. Figure 8 presents information on the cell tumbling and tank-treading frequencies under different conditions. Experimental observations by Tran-Son-Tay et al.[30] and Fischer[32] are included for comparison. In the case of a purely elastic membrane with or without inner solvent (circles and squares), the numerical results significantly overpredict the tank-treading frequency compared with experimental measurements. The internal solvent viscosity could be further increased to improve agreement with experimental data. However, since the cytosol is a hemoglobin solution with a well-defined viscosity of about $0.005\ Pa \cdot s$[33], excess viscous dissipation must occur inside the membrane. The data plotted with triangles in figure 8 show good agreement with experimental data for increased membrane viscosity.

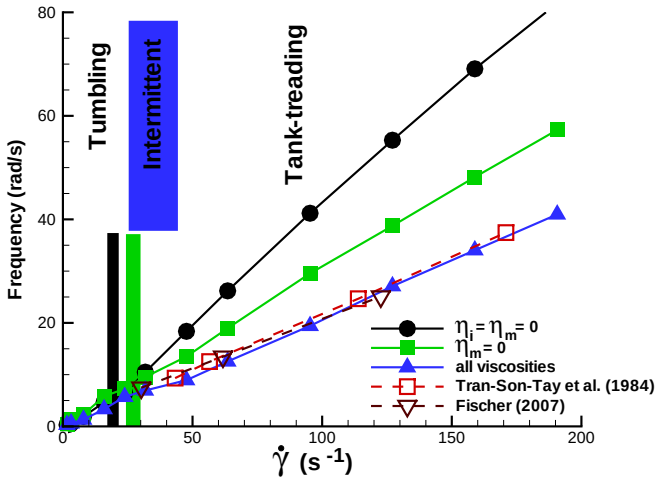

Figure 8. Tumbling and tank-treading frequency of a RBC in shear flow for $\eta_o = 0.005\ Pa \cdot s$, $\eta_i = \eta_m = 0$ (circles); $\eta_o = \eta_i = 0.005\ Pa \cdot s$, $\eta_m = 0$ (squares); $\eta_o = \eta_i = 0.005\ Pa \cdot s$, $\eta_m = 0.022\ Pa \cdot s$ (triangles).

The tumbling frequency is nearly independent of the medium viscosities. Increasing the viscosity of the internal fluid or raising the membrane viscosity slightly shifts the tumbling-to-treading threshold into higher shear rates through an intermittent regime. We estimate that the tank-treading energy barrier of a cell is approximately $E_c = 3$ to $3.5 \times 10^{-17}\ J$. In the theoretical model[9], the energy barrier was set to $E_c = 10^{-17}\ J$ to ensure agreement with experimental data. Membrane deformation during tank treading is indicated by an increase in the elastic energy difference with increasing shear rate to within about 20% of E_c.

An intermittent regime is observed with respect to the shear rate in all cases. Consistent with the experiments, the width of the transition zone broadens as the membrane viscosity increases. Similar results regarding intermittency were reported by Kessler et al.[34] for viscoelastic vesicles. We conclude that theoretical predictions of cell dynamics in shear flow are qualitatively correct at best due to the assumption of ellipsoidal shape and fixed ellipsoidal tank-treading path. Experiments[8] have shown and the present simulations have confirmed that the cell deforms along the tank-treading axis with strains of order $0.1-0.15$.

We have seen that a cell oscillates or swings around tank-treading axes with a certain frequency and amplitude. Figure 9 presents graphs of the average tank-treading angle and swinging amplitude. The numerical results are consistent with experimental data in Ref.[8]. The average swinging angle is larger for a purely elastic membrane without inner cytosol. The inclination angle is independent of the internal fluid and membrane viscosities and the swinging amplitude is insensitive to the fluid and membrane properties. The swinging frequency is exactly twice the tank-treading frequency.

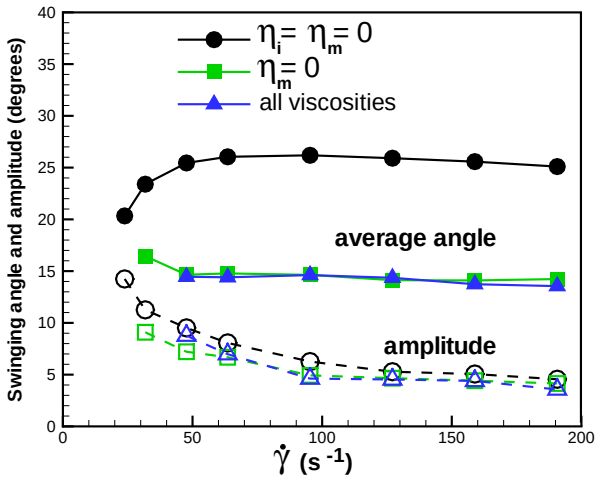

Figure 9. Graphs of the swinging average angle in degrees (filled symbols) and amplitude (open symbols) for (*a*) $\eta_o = 0.005\ Pa \cdot s$ and $\eta_i = \eta_m = 0$ (circles); (*b*) $\eta_o = \eta_i = 0.005\ Pa \cdot s$ and $\eta_m = 0$ (squares); (*c*) $\eta_o = \eta_i = 0.005\ Pa \cdot s$ and $\eta_m = 0.022\ Pa \cdot s$ (triangles).

4.3 Blood viscosity

Blood viscosity was computed, with and without aggregation, as a function of the shear rate $\dot{\gamma}$ over the range $0.005s^{-1}$ to $1000.0s^{-1}$ in plane Couette flow. The shear rate and the cell density in our simulations were verified to be spatially uniform. Figure 10 shows the relative viscosity (RBC suspension viscosity normalized by η_0) against shear rate $\dot{\gamma}$ at hematocrit $H_t = 0.45$. The blood model predictions are in excellent agreement with the blood viscosities measured in three different laboratories[1–3]. The blood model, consisting only of RBCs in suspension, clearly captures the effect of aggregation on the viscosity at low shear rates, and suggests that cells and molecules other than RBCs have little effect on the viscosity, at least under healthy conditions. At intermediate shear rates, where aggregation is no longer relevant, shear thinning is due to a transition from tumbling to tank-treading motion, accompanied by strong cell deformations[20].

4.4 Reversible rouleaux formation

The formation of rouleaux in blood occurs in equilibrium and at sufficiently small shear rates, while large shear rates result in immediate dispersion of gentle RBC structures. Experimentally, aggregation is observed[1] to be a two-step process: the formation of short linear stacks with few RBCs, followed by their coalescence into long linear and branched rouleaux. As the shear rate increases the large rouleaux break up into smaller ones, and at higher values the suspension ultimately becomes one of mono-dispersed RBCs[35]. This process then reverses as the shear rate is decreased. This typical formation-destruction behavior of rouleaux is consistent with the results of our simulations as shown in figure 11.

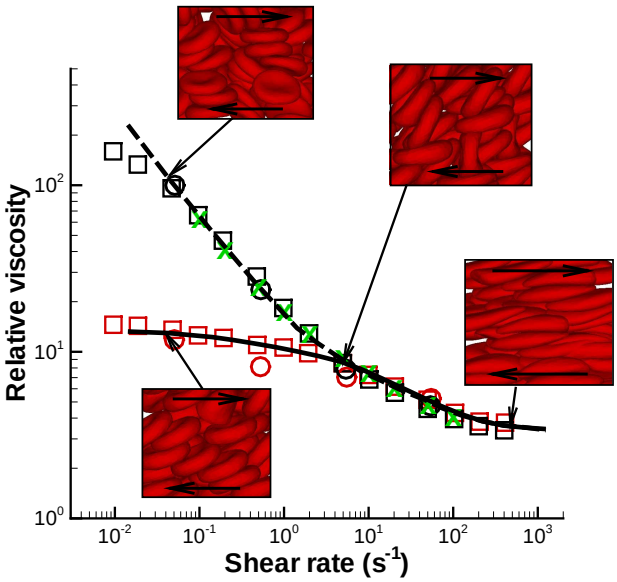

Figure 10. Validation of simulation results for whole blood and non-aggregating RBC suspension. Plot of non-Newtonian relative viscosity (the cell suspension viscosity normalized by η_0) as a function of shear rate at $H_t = 0.45$ and 37^oC: *simulated* curves are in black, and *experimental* points: Whole blood: green crosses - Merril et al.[1]; black circles - Chien et al.[2], black squares - Skalak et al.[3]. Non-aggregating RBC suspension: red circles - Chien et al.[2]; red squares - Skalak et al.[3].

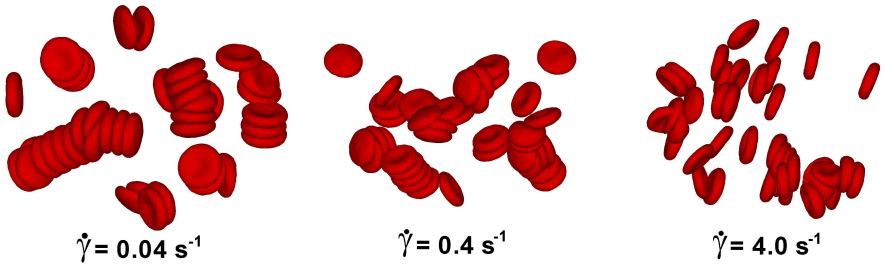

Figure 11. Visualization of aggregation. Simulated reversible rouleaux are formed by RBCs at $H_t = 0.1$. The left plot corresponds to low shear rates, middle plot to moderate share rates, and right plot to high shear rates as indicated with the shear rate values.

At low shear rates (left plot), the initially dispersed RBCs aggregate into large rouleaux of up to about 20 RBCs; as the shear rate is increased to moderate values (middle plot), these structures are reduced in size until at high rates (right plot) they are dispersed almost completely into individual RBCs. Reversibility is demonstrated by reduction of the shear rate to the formation value at which point individual RBCs begin to re-aggregate.

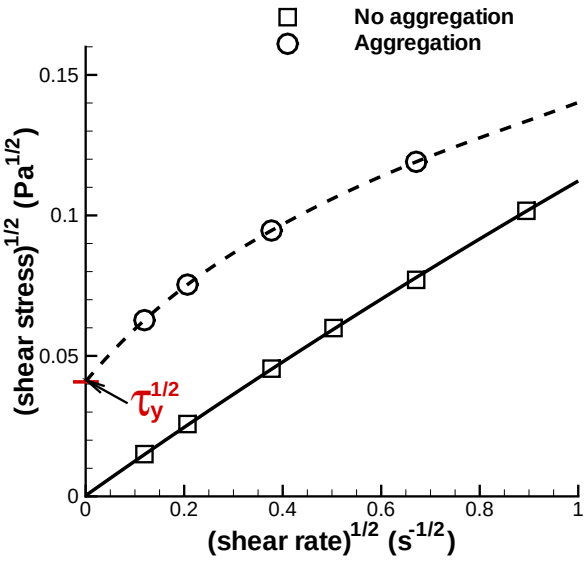

Figure 12. Correlation of aggregation with yield stress. Casson plots with a polynomial fit showing the extrapolated intercept τ_y for simulated suspensions with, dashed lines, and without aggregation, solid lines, at $H_t = 0.45$.

4.5 Yield stress and aggregation

Whole blood is believed to exhibit a yield stress, i.e. a threshold stress for flow to begin[1,6,7], which is often estimated by the extrapolation of measured shear stress to the zero shear rate on the basis of the Casson's equation[36],

$$\tau_{xy}^{1/2} = \tau_y^{1/2} + \eta^{1/2}\dot{\gamma}^{1/2}, \tag{29}$$

where τ_y is a yield stress and η is the suspension viscosity at large $\dot{\gamma}$. The assumptions of Casson's relation are likely to hold at least at low shear rates, which was successfully demonstrated for pigment-oil suspensions[36], Chinese ovary hamster cell suspensions[37], and blood[4]. Figure 12 is a polynomial fit in Casson coordinates ($\dot{\gamma}^{1/2}$,$\tau_{xy}^{1/2}$) to the simulated data for a $H_t = 0.45$ suspension, which shows clearly that τ_y is non-zero for the aggregating RBC suspension, while τ_y is absent without cell aggregation. The yield stress for blood has previously been attributed to the presence of rouleaux in experiments reported in Refs.[1,6,7]. Merrill et al.[1] found τ_y of healthy human blood to lie between 0.0015 and $0.005\ Pa$ at $H_t = 0.45$. Our simulation results in figure 12 fall into this range of the yield stress of whole blood.

4.6 Micro-to-macro link.

The non-Newtonian nature of blood (e.g., shear thinning, yield stress) emerges from the interactions between cells and from their properties and dynamics. Therefore, we examined the structure and dynamics of the modeled suspensions on the level of single cells.

We found null pair-correlations of RBC *centers of mass* for each direction (x, y, z), which indicates that the cell suspensions do not self-assemble or order themselves in any direction at $H = 45\%$. To examine the cell suspension's local microstructure, we calculate the radial distribution function (RDF) of RBC centers shown in figure 13(a). For the no-

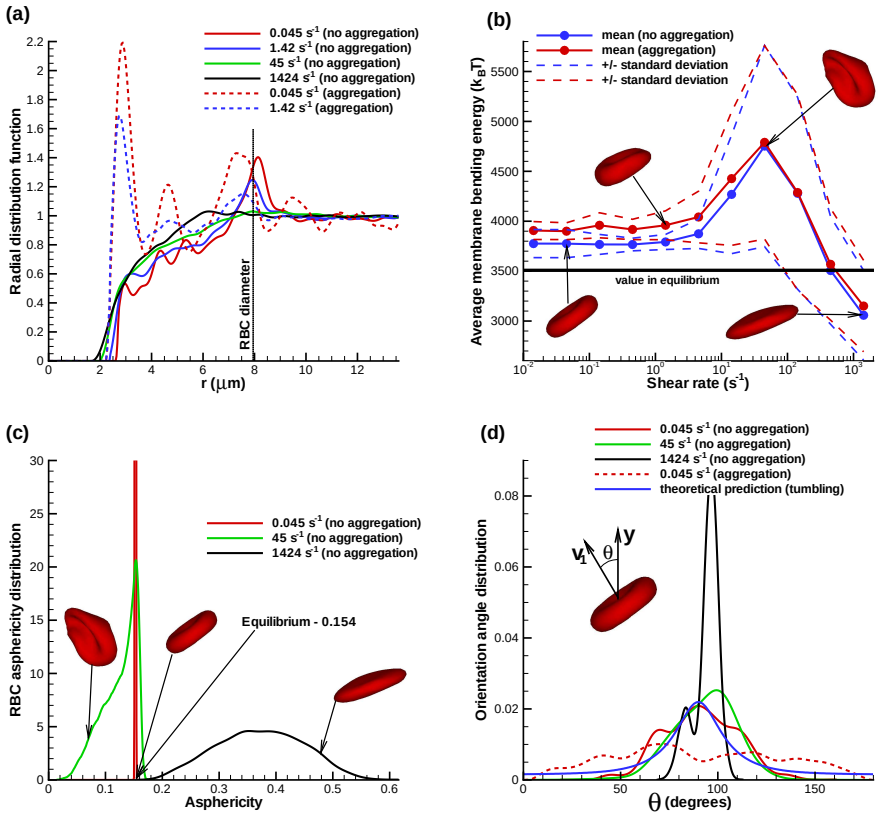

Figure 13. Structural and dynamical properties of RBC suspensions with $H = 45\%$. Snapshots show sample RBC conformations from simulations. (a) Radial distribution function showing cell suspension's structure. (b) Average membrane bending energy with respect to shear rate showing correlation between single cell deformation and dynamics. Dashed lines are the corresponding mean values plus/minus one standard deviation. (c) RBC asphericity distributions characterizing the deviation from a spherical shape as a function of shear rate. The asphericity is defined as $[(\lambda_1 - \lambda_2)^2 + (\lambda_2 - \lambda_3)^2 + (\lambda_3 - \lambda_1)^2]/(2R_g^4)$, where $\lambda_1 \leq \lambda_2 \leq \lambda_3$ are the eigenvalues of the gyration tensor and $R_g^2 = \lambda_1 + \lambda_2 + \lambda_3$. The asphericity for a single RBC in equilibrium is equal to 0.154. (d) Orientational angle distributions for various shear rates which illustrate single cell dynamics. The cell orientational angle is given by the angle between the eigenvector V_1 of the gyration tensor and the flow-gradient direction (y). Theoretical prediction showing the orientational angle distribution of a single tumbling RBC in shear flow is calculated from the theory in Ref.[8].

aggregation case, we find that no significant structures formed over the entire range of shear rates. At the lowest shear rate (red solid line) several small peaks in RDF indicate the presence of infrequent intermediate structures, since RBCs may have enough time to

relax locally at very low shear rates. A larger peak of the red solid curve at $r = 8\mu m$, which is equal to the cell diameter, indicates that neighboring RBCs are often aligned with each other in the flow. As seen from the other solid curves (blue, green, and black), the correlations completely disappear at higher shear rates, and therefore the shear thinning behavior of a non-aggregating suspension is clearly not due to a change in microstructure. In contrast, several large peaks in the RDF function for the aggregating case at the lowest shear rate $\dot{\gamma} = 0.045\ s^{-1}$ (red dashed line) indicate the formation of rouleaux of 2 to 4 RBCs. Increase of the shear rate leads to the dispersion of rouleaux shown by the blue dashed curve in figure 13(a), where predominant RBC aggregates are formed by only two RBCs. At shear rates above approximately $5 - 10\ s^{-1}$ no difference in microstructure is detected between aggregating and non-aggregating cell suspensions. As a conclusion, the steep increase in viscosity of the aggregating blood at low shear rates is mainly due to the cell aggregation into rouleaux. In addition, rouleaux formation also provides a plausible explanation for the existence of yield stress, since with decrease of shear rate larger rouleaux structures are formed resulting in an eventual "solidification" of the suspension.

The dynamics of a single RBC in shear flow is characterized by the tumbling motion at low shear rates and membrane tank-treading at high shear rates[8,15,16]. The tumbling-to-tank-treading transition occurs within a certain range of intermediate shear rates, where a RBC may experience high bending deformations[16]. The deformation, orientation, and dynamics of cells within the suspension is illustrated in figures 13(b), (c), and (d). These plots show that cells in the suspension mostly tumble and retain their biconcave shape at low shear rates below $5\ s^{-1}$, which is confirmed by essentially no change in RBC bending energy and in its standard deviation (figure 13(b)), by the extremely narrow asphericity distribution around the equilibrium value of 0.154 (figure 13(c)), and by the wide orientational angle (θ) distribution in figure 13(d). Cell tumbling at low shear rates is slightly hindered in non-aggregating suspensions in comparison to tumbling of a single RBC in shear flow due to cell crowding, which results in sliding of cells over each other; this is shown by a higher peak in the orientational angle distribution (green curve) in figure 13(d) with respect to the theoretical prediction (blue curve). In contrast, RBC tumbling in aggregating suspensions appears to be nearly uniform, since RBCs tumble within multiple-cell rouleaux structures. At high shear rates, larger than about $200\ s^{-1}$, individual RBCs are subject to tank-treading motion illustrated by a narrow θ distribution (black line) in figure 13(d). At yet higher shear rates RBCs become strongly elongated as indicated by the RBC asphericity distribution in figure 13(c).

The most interesting and complex cell dynamics, however, occurs in the broad intermediate regime of shear rates between $5\ s^{-1}$ and $200\ s^{-1}$, where RBC aggregation interactions can be neglected. This range also corresponds to the main region of shear thinning for the non-aggregating cell suspension. In this range of shear rates, RBCs within the suspension experience severe deformations documented by a pronounced increase in the membrane bending energy and in its variation shown in figure 13(b). The asphericity distribution for $\dot{\gamma} = 45\ s^{-1}$ in figure 13(c) shows that RBCs attain on average a more spherical shape indicating transient folded conformations. This may result in a reduction of shear stresses due to collisional constraints of cell tumbling, and therefore in shear thinning. In addition, the transition of some cells to the tank-treading motion further reduces the shear stresses contributing to the viscosity thinning.

5 Summary

We have presented a mesoscopic model of RBCs implemented by the dissipative particle dynamics method. The spectrin cytoskeleton is represented by a network of interconnected viscoelastic springs comprising a membrane with elastic and viscous properties. The surface network accounts for bending resistance attributed to the lipid bilayer and incorporates local and global area constraints to ensure constant volume and surface area. The macroscopic properties of the membrane were related to the network parameters by theoretical analysis. RBC dynamics was simulated in shear flow, where a cell exhibits tumbling at low shear rates and tank-treading at high shear rates. A narrow intermittent region appears where these modes interchange. The model is able to quantitatively capture cell dynamics in shear flow. Comparison of the numerical results with existing theoretical predictions suggest that the latter suffers from oversimplification .

Results on the rheological properties of human blood suggest that the RBC suspension model is able to accurately predict shear-dependent viscosity of blood with and without aggregation interactions between RBCs. The RBC aggregation model was able to properly capture the assembly of RBCs into rouleaux structures. These simulations also confirmed that whole blood is a fluid with a non-zero yield stress. We have shown how single RBC characteristics and behavior contribute to the macroscopic properties of blood, which may not be possible to elucidate in experiments. The predictive capability of the current cell/capsule suspension model can readily be extended to a variety of engineering and material science applications, which may aid in the development of new soft materials. Finally, such simulations of soft capsule suspensions are computationally demanding and are only feasible on massively parallel computers.

Acknowledgments

We would like to thank Gerhard Gompper, Bruce Caswell, and George E. Karniadakis for many fruitful discussions. Dmitry A. Fedosov acknowledges funding by the Humboldt Foundation. The computations were performed on JUROPA with a grant of computer time provided by the VSR of the Research Centre Jülich.

Appendix

A Dissipative particle dynamics

Dissipative particle dynamics (DPD)[21,38] is a mesoscopic particle method, where each particle represents a *molecular cluster* rather than an individual atom, and can be thought of as a soft lump of fluid. The DPD system consists of N point particles of mass m_i, position $\mathbf{r}_i$ and velocity $\mathbf{v}_i$. DPD particles interact through three forces: conservative ($\mathbf{F}^C_{ij}$), dissipative ($\mathbf{F}^D_{ij}$), and random ($\mathbf{F}^R_{ij}$) forces given by

$$\mathbf{F}^C_{ij} = F^C_{ij}(r_{ij})\hat{\mathbf{r}}_{ij}, \quad \mathbf{F}^D_{ij} = -\gamma\omega^D(r_{ij})(\mathbf{v}_{ij}\cdot\hat{\mathbf{r}}_{ij})\hat{\mathbf{r}}_{ij}, \quad \mathbf{F}^R_{ij} = \sigma\omega^R(r_{ij})\frac{\xi_{ij}}{\sqrt{dt}}\hat{\mathbf{r}}_{ij}, \quad (30)$$

where $\hat{\mathbf{r}}_{ij} = \mathbf{r}_{ij}/r_{ij}$, and $\mathbf{v}_{ij} = \mathbf{v}_i - \mathbf{v}_j$. The coefficients γ and σ define the strength of dissipative and random forces, respectively. In addition, ω^D and ω^R are weight functions,

and ξ_{ij} is a normally distributed random variable with zero mean, unit variance, and $\xi_{ij} = \xi_{ji}$. All forces are truncated beyond the cutoff radius r_c. The conservative force is given by

$$F_{ij}^C(r_{ij}) = a_{ij}(1 - r_{ij}/r_c) \quad \text{for} \quad r_{ij} \leq r_c, \tag{31}$$

where a_{ij} is the conservative force coefficient between particles i and j. The random and dissipative forces form a thermostat and must satisfy the fluctuation-dissipation theorem in order for the DPD system to maintain equilibrium temperature T[39]. This leads to

$$\omega^D(r_{ij}) = \left[\omega^R(r_{ij})\right]^2, \qquad \sigma^2 = 2\gamma k_B T, \tag{32}$$

where k_B is the Boltzmann constant. The choice for the weight functions is as follows

$$\omega^R(r_{ij}) = (1 - r_{ij}/r_c)^k \quad \text{for} \quad r_{ij} \leq r_c, \tag{33}$$

where k is an exponent. The time evolution of velocities and positions of particles is determined by the Newton's second law of motion

$$d\mathbf{r}_i = \mathbf{v}_i dt, \qquad d\mathbf{v}_i = \frac{1}{m_i} \sum_{j \neq i} \left(\mathbf{F}_{ij}^C + \mathbf{F}_{ij}^D + \mathbf{F}_{ij}^R\right) dt. \tag{34}$$

The above equations of motion are integrated using the modified velocity-Verlet algorithm[38].

References

1. E. W. Merrill, E. R. Gilliland, G. Cokelet, H. Shin, A. Britten, and JR. R. E. Wells, *Rheology of human blood near and at zero flow*, Biophys. J., **3**, 199–213, 1963.
2. S. Chien, S. Usami, H. M. Taylor, J. L. Lundberg, and M. I. Gregersen, *Effects of hematocrit and plasma proteins on human blood rheology at low shear rates*, J. App. Physiol., **21**, no. 1, 81–87, 1966.
3. R. Skalak, S. R. Keller, and T. W. Secomb, *Mechanics of blood flow*, J. Biomech. Engin., **103**, 102–115, 1981.
4. E. W. Merrill, E. R. Gilliland, T. S. Lee, and E. W. Salzman, *Blood Rheology: Effect of Fibrinogen Deduced by Addition*, Circ. Res., **18**, 437–446, 1966.
5. S. Chien, S. Usami, R. J. Kellenback, and M. I. Gregersen, *Shear-dependent interaction of plasma proteins with erythrocytes in blood rheology*, Am. J. Physiol., **219**, no. 1, 143–153, 1970.
6. G. Cokelet, E. W. Merrill, E. R. Gilliland, H. Shin, A. Britten, and JR. R. E. Wells, *The rheology of human blood-measurement near and at zero shear rate*, Transaction of the Society of Rheology, **7**, 303–317, 1963.
7. A. L. Copley, C. R. Huang, and R. G. King, *Rheogoniometric studies of whole human blood at shear rates from 1,000-0.0009* $\sec^{-1}$. *Part I. Experimental findings*, Biorheology, **10**, 17–22, 1973.
8. M. Abkarian, M. Faivre, and A. Viallat, *Swinging of red blood cells under shear flow*, Phys. Rev. Lett., **98**, 188302, 2007.
9. J. M. Skotheim and T. W. Secomb, *Red blood cells and other nonspherical capsules in shear flow: Oscillatory dynamics and the tank-treading-to-tumbling transition*, Phys. Rev. Lett., **98**, 078301, 2007.

10. Y. C. Fung, *Biomechanics: Mechanical properties of living tissues*, Springer-Verlag, New York, second edition, 1993.
11. C. D. Eggleton and A. S. Popel, *Large deformation of red blood cell ghosts in a simple shear flow*, Phys. Fluids, **10**, no. 8, 1834, 1998.
12. C. Pozrikidis, *Numerical Simulation of Cell Motion in Tube Flow*, Ann. Biomed. Engin., **33**, no. 2, 165–178, 2005.
13. H. Noguchi and G. Gompper, *Shape transitions of fluid vesicles and red blood cells in capillary flows*, Proc. Natl. Acad. Sci. USA, **102**, no. 40, 14159–14164, 2005.
14. M. M. Dupin, I. Halliday, C. M. Care, L. Alboul, and L. L. Munn, *Modeling the flow of dense suspensions of deformable particles in three dimensions*, Phys. Rev. E, **75**, no. 6, 066707, 2007.
15. I. V. Pivkin and G. E. Karniadakis, *Accurate coarse-grained modeling of red blood cells*, Phys. Rev. Lett., **101**, no. 11, 118105, 2008.
16. D. A. Fedosov, B. Caswell, and G. E. Karniadakis, *A multiscale red blood cell model with accurate mechanics, rheology, and dynamics*, Biophys. J., **98**, no. 10, 2215–2225, 2010.
17. Y. Liu and W. K. Liu, *Rheology of red blood cell aggregation by computer simulation*, J. Comp. Phys., **220**, 139–154, 2006.
18. J. L. McWhirter, H. Noguchi, and G. Gompper, *Flow-induced clustering and alignment of vesicles and red blood cells in microcapillaries*, Proc. Natl. Acad. Sci. USA, **106**, no. 15, 6039–6043, 2009.
19. J. B. Freund and M. M. Orescanin, *Cellular flow in a small blood vessel*, J. Fluid Mech., **671**, 466–490, 2011.
20. D. A. Fedosov, B. Pan, W. Caswell, G. Gompper, and G. E. Karniadakis, *Predicting human blood viscosity in silico*, Proc. Natl. Acad. Sci. USA, **108**, 11772–11777, 2011.
21. P. J. Hoogerbrugge and J. M. V. A. Koelman, *Simulating microscopic hydrodynamic phenomena with dissipative particle dynamics*, Europhys. Lett., **19**, no. 3, 155–160, 1992.
22. D. E. Discher, D. H. Boal, and S. K. Boey, *Simulations of the erythrocyte cytoskeleton at large deformation. II. Micropipette aspiration*, Biophys. J., **75**, no. 3, 1584–1597, 1998.
23. D. A. Fedosov, B. Caswell, and G. E. Karniadakis, *Systematic coarse-graining of spectrin-level red blood cell models*, Computer Meth. Appl. Mech. Engin., **199**, 1937–1948, 2010.
24. P. Espanol, *Fluid particle model*, Phys. Rev. E, **57**, no. 3, 2930–2948, 1998.
25. M. Dao, J. Li, and S. Suresh, *Molecularly based analysis of deformation of spectrin network and human erythrocyte*, Materials Sci. Engin. C, **26**, 1232–1244, 2006.
26. M. P. Allen and D. J. Tildesley, *Computer Simulation of Liquids*, Clarendon Press, Oxford, 1987.
27. W. Helfrich, *Elastic properties of lipid bilayers: theory and possible experiments*, Z. Naturforschung C, **28**, 693–703, 1973.
28. J. Lidmar, L. Mirny, and D. R. Nelson, *Virus shapes and buckling transitions in spherical shells*, Phys. Rev. E, **68**, no. 5, 051910, 2003.
29. A. W. Lees and S. F. Edwards, *The computer study of transport processes under extreme conditions*, J. Phys. C, **5**, 1921–1928, 1972.

30. R. Tran-Son-Tay, S. P. Sutera, and P. R. Rao, *Determination of RBC membrane viscosity from rheoscopic observations of tank-treading motion*, Biophys. J., **46**, no. 1, 65–72, 1984.
31. T. M. Fischer, *Shape memory of human red blood cells*, Biophys. J., **86**, no. 5, 3304–3313, 2004.
32. T. M. Fischer, *Tank-Tread Frequency of the Red Cell Membrane: Dependence on the Viscosity of the Suspending Medium*, Biophys. J., **93**, no. 7, 2553–2561, 2007.
33. G. R. Cokelet and H. J. Meiselman, *Rheological comparison of hemoglobin solutions and erythrocyte suspensions*, Science, **162**, 275–277, 1968.
34. S. Kessler, R. Finken, and U. Seifert, *Swinging and tumbling of elastic capsules in shear flow*, J. Fluid Mech., **605**, 207–226, 2008.
35. Q. Zhao, L. G. Durand, L. Allard, and G. Cloutier, *Effects of a sudden flow reduction on red blood cell rouleau formation and orientation using RF backscattered power*, Ultrasound Med. Biol., **24**, 503–511, 1998.
36. N. Casson, "A flow equation for pigmented oil suspension of printing ink", in: Rheology of Disperse Systems, C. C. Mill, (Ed.), pp. 84–104. Pergamon Press, New York, 1992.
37. A. Iordan, A. Duperray, and C. Verdier, *Fractal approach to the rheology of concentrated suspensions*, Phys. Rev. E, **77**, 011911, 2008.
38. R. D. Groot and P. B. Warren, *Dissipative particle dynamics: Bridging the gap between atomistic and mesoscopic simulation*, J. Chem. Phys., **107**, no. 11, 4423–4435, 1997.
39. P. Espanol and P. Warren, *Statistical mechanics of dissipative particle dynamics*, Europhys. Lett., **30**, no. 4, 191–196, 1995.